

New Insight Into Wormhole Formation in Polymer Gel During Water Chase Floods With Positron Emission Tomography

B. Brattekkås, University of Stavanger; M. Steinsbø, A. Graue, M. A. Fernø, and H. Espedal, University of Bergen; and R. S. Seright, New Mexico Petroleum Recovery Research Center

Summary

Polymer gel is frequently used for conformance control in fractured reservoirs, where it is injected to reside in fractures or high-permeability streaks to reduce conductivity. With successful polymer-gel conformance control in place, increased pressure gradients across matrix blocks may be achieved during chase floods, diverting water, gas, or enhanced oil recovery (EOR) chemicals into the matrix to displace oil. Knowledge of gel behavior during placement and chase floods is important because it largely controls the success of subsequent injections. Polymer-gel behavior is often studied in corefloods, where differential pressure and effluents from fracture and matrix outlets give information about gel deposition during placement and flow paths during chase floods. The work presented in this paper uses complementary positron emission tomography (PET) chromatographic tomography (CT) imaging to quantify the behavior and blocking capacity of Cr(III)-acetate hydrolyzed polyacrylamide (HPAM) gel during chase waterflooding. In-situ imaging provides information about changes that may not be extracted from pressure measurements and material balance only, such as changes in local fluid saturations and dynamic spatial flow within the fracture and within the structure of the gel network.

Polymer gel was placed in core plugs with longitudinal fractures that connected the inlet and outlet, and chase water was subsequently injected to measure the gel blocking capacity. The water phase was labeled with a positron emitting radiopharmaceutical (F-18) to visualize and quantify local flows with PET during gel rupture and subsequent flooding. By use of PET, we study gel rupture and the development of wormholes during gel erosion after rupture as a function of flow rate. A particular strength with access to dynamic, local flow patterns is the direct comparison to global measurements, such as differential pressure and production rate, to verify existing gel-behavior models.

Introduction

Fractures in a hydrocarbon reservoir often exhibit permeabilities several orders of magnitude higher than that of the rock matrix, and heavily influence fluid flow. Injected fluids and gases may channel through the fractures without contacting large volumes of matrix oil, which causes poor microscopic and macroscopic sweep efficiencies, and hence low oil-recovery factors. The main challenge during EOR operations in fractured reservoirs is to prevent fracture channeling, so that injected fluids and gases can contact and displace the oil in the matrix. Channeling of injected fluids through a high-permeability fracture network, and the following early fluid breakthrough, may be mitigated by placing a highly viscous polymer gel in the fracture (Portwood 1999; Seright et al. 2003; Willhite and Pancake 2008). With polymer gel in place, higher differential pressures may be achieved during chase floods and contribute to increased sweep efficiency in the

porous matrix adjacent to the fracture network. Gel placement in fractures and gel-blocking capacity during chase floods have been thoroughly investigated and discussed in the literature (e.g., Ganguly et al. 2002; Seright 2003a, 2003b; Brattekkås et al. 2015a, 2015b). A polymer gel is formed when a gelant solution (a mixture containing all the chemical components needed to form a polymer gel) is exposed to elevated temperature for a given time known as the gelation time. Previous work investigated how the gel state during placement (gel or gelant) influenced the gel behavior during chase floods (Brattekkås et al. 2015a, 2015b). In this work, we study the extrusion of formed polymer gel through fractures and its resistance to pressure during subsequent waterfloods.

Formed gel is highly viscous, and its structure prevents it from entering significantly into the porous matrix next to the fracture during placement. The gel solvent (water in most cases) may, however, leave the gel during propagation through the fracture and progress into the matrix in a leakoff process. During water leakoff, a filter cake of concentrated gel forms in the fracture. The concentrated gel is more rigid compared with the injected gel, and is more pressure-resistant. The rate of water leakoff has implications for the rate of gel propagation into a fractured reservoir, as well as the rate of fracture growth during hydraulic fracturing, and was previously investigated by Carter (Howard and Fast 1957, 1970; Penny and Conway 1989) and Seright (1999, 2001, 2003a, 2003b). Carter proposed a model for fluid leakoff during hydraulic fracturing, in which an important assumption was that the thickness of the filter cake on the fracture faces was uniform at any given time. Seright (2003b) presented an alternative model for leakoff, suggesting that the filter cake on the fracture wall was areally and volumetrically heterogeneous, and formed when fragments of injected gel dehydrated and became immobile in the vicinity where the dehydration occurred. Mobile gel of the original composition flowed through the concentrated gel to advance to the gel front within narrow flow channels, termed wormholes. The term wormholes was previously used, and will be used in this work, to denote a part of the fracture volume that (a) is filled with nondehydrated gel of injected composition during and after gel placement and (b) represents the path of rupture and subsequently conducts the flow of fluids during chase floods. According to the Seright leakoff model, the dehydrated-gel filter cake surrounds the wormholes in the fracture. Because of the elastic nature of the filter cake, wormholes have the ability to collapse and reopen during chase floods, depending on the applied pressure gradient. The proposed leakoff models by Seright and Carter were similar in terms of leakoff rate; however, the filter-cake formation within the fracture was suggested to take place in widely different manners, and is an important distinction that strongly influences fluid flow during chase floods. **Fig. 1** illustrates filter-cake formation during, and because of, water leakoff for the two models: the Carter model on the left, with the filter cake forming on the fracture surfaces only, and the Seright model on the right, with a randomly distributed filter cake forming in the fracture volume.

Brattekkås et al. (2015a, 2015b) showed, by use of pressure measurements, that gel resistance during waterflooding was higher in cores after formed-gel placement compared with gelant placement with following in-situ crosslinking. This was explained by the gel's ability to form wormholes through a filter cake during

Copyright © 2017 Society of Petroleum Engineers

This paper (SPE 180051) was accepted for presentation at the SPE Bergen One Day Seminar, Grieghallen, Bergen, Norway, 20 April 2016, and revised for publication. Original manuscript received for review 5 February 2016. Revised manuscript received for review 6 May 2016. Paper peer approved 11 May 2016.

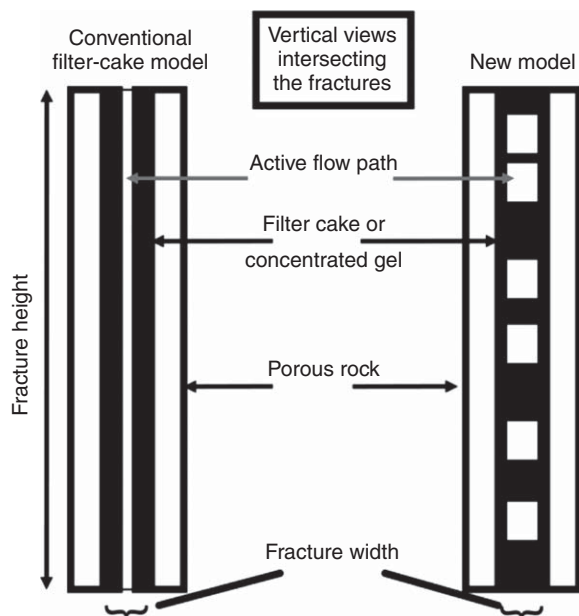


Fig. 1—Seright (2003b) illustrated filter-cake formation in each of the two leakoff models: Left: leakoff model by Carter; Right: leakoff model by Seright. The view is into the cross section of an open fracture.

placement: Formed gel dehydrates during propagation through a fracture, which increases its pressure resistance, and fresh gel flows through the concentrated gel in wormholes. During chase waterflooding, fresh gel is displaced from the wormholes at the rupture pressure, and water follows these narrow flow paths through the fracture volume. Flow of water through wormholes at the rupture pressure may be viewed as a case of viscous fingering (Benham and Olson 1963), where the development of the viscous finger (the wormhole flow pattern) is caused by the large mobility contrast between the dehydrated-gel filter cake and the relatively mobile gel contained in the wormholes. As long as the injected water is contained in wormholes during chase floods, fracture permeability remains significantly decreased. During placement of gel in its immature form (as a gelant), and according to the Carter filter-cake model for formed-gel placement, wormholes do not form. Consequently, gel erosion during waterflooding occurs in a different manner, and may open larger sections of the fracture to flow. Visualization of gel placement and chase waterfloods in fractures can be achieved with see-through acrylic glass models (e.g., Liu 2006)); however, the formation and development of wormholes through a fracture depend on the presence of a porous medium directly adjacent to the fracture. Observations of wormholes in opaque core-plug systems have previously been described: Seright (2003b) injected dyed gel to follow gel of the same composition (not dyed) into a fracture, and could thus visualize the formation of wormholes during gel injection. After chase waterflooding, wormhole patterns can be clearly visible when opening the used core and inspecting the fracture surfaces (Bratte-kås et al. 2015a, 2015b). The development of wormholes during dynamic chase waterfloods in opaque systems has, however, only been investigated through global measurements of pressure and flow rate. In this study, we used PET to identify this phenomenon in situ. PET imaging is based on the decay of positron-emitting radionuclides. The positron loses kinetic energy by interactions with the surroundings, and at near-zero momentum, the positron is emitted from the nucleus accompanied by an electron to balance atomic charge. Radioactivity is a spontaneous nuclear phenomenon that is insensitive to temperature and pressure (Erslund et al. 2010). PET is a frequently used method for medical in-situ imaging. In oil-and-gas-related research, PET was recently used to study flow in tight rock samples (and the results were compared with CT imaging) (Fernø et al. 2015a, 2015b), to study fluid mo-

bility in fractures (Maucec et al. 2013), and to visualize the displacement front during spontaneous imbibition applying two-open-ends- (TEO-) free boundary conditions (Fernø et al. 2015a, 2015b). In this work, PET was used to visualize flow of radioactive water through a gel-filled fracture, to augment global measurements, and to increase the understanding of filter-cake formation during formed-gel placement and wormhole development during chase floods.

Experimental Section

Experimental Schedule. The experimental schedule consisted of three steps: (1) core-plug preparation, (2) polymer-gel placement, and (3) chase waterflooding to measure gel-blocking capacity and to investigate the development of wormholes. In-situ imaging by PET was used during Step 3 to visualize and quantify the flow of water through a gel-filled fracture.

Core-Plug Preparation. Highly heterogeneous outcrop limestone from the Edwards formation in Texas, USA, with trimodal pore sizes, vugs, and microporosity (Ekdale and Bromley 1983; Siddhartha and Morrow 2007), and homogeneous sandstone from the Gildenhause quarry in Bentheimer, Germany (Schutjens et al. 1995; Klein and Reuschle 2003), was used to study chaseflood behavior through gel-filled fractures (the results for the sandstone core plug are previously published in Bratte-kås et al. 2015a).

Cylindrical core plugs with 4.96-cm diameter were drilled from larger outcrop limestone and sandstone blocks and cut to length ($L_{\text{limestone}} = 7.56$ cm and $L_{\text{sandstone}} = 10.12$ cm). Smooth, longitudinal fractures were created through the cores with a band saw, and the core surfaces were gently washed with tap water to remove loose grains. The core fragments were dried at an elevated temperature of 60 °C for 1 week. Fractured cores were assembled with clamps and POM (polyoxymethylene) spacers to maintain a constant fracture aperture of 1 mm. Surfaces were covered in epoxy resin, and only the fracture surfaces were left open to flow. POM end pieces were designed, featuring three inlets and three outlets, separating the fracture from each matrix core half. The end pieces were glued to the core inlet and outlet end faces with epoxy resin. After drying, holes were drilled through the epoxy into the matrix core halves to allow flow. The assembled cores were covered in several layers of epoxy resin to increase the resistance to flow, and could thus be used in flooding experiments with no additional overburden pressure. The core plugs were saturated with brine (4 wt% NaCl, 3.4 wt% $\text{MgCl}_2 \cdot 6\text{H}_2\text{O}$, 0.5 wt% $\text{CaCl}_2 \cdot 2\text{H}_2\text{O}$) after assembly, and porosity was calculated from weight measurements.

Polymer-Gel Placement. The 0.5% HPAM polymer (≈ 5 million Daltons molecular weight) and 0.0417 wt% Cr(III)-acetate were mixed in brine (4 wt% NaCl, 3.4 wt% $\text{MgCl}_2 \cdot 6\text{H}_2\text{O}$, 0.5 wt% $\text{CaCl}_2 \cdot 2\text{H}_2\text{O}$) to form gelant. After thorough mixing, the gelant solution was placed in a stainless-steel accumulator and aged at 41 °C for 24 hours (five times the gelation time) to form mature polymer gel. The gel was allowed to cool to ambient conditions (approximately 23 °C) before injection into the fractured core plugs, with injection rates of 200 cm^3/h (limestone) and 6 cm^3/h (sandstone). Leakoff was recorded by volumetric measurements of brine effluent exiting the matrix outlets as a function of time. After gel placement, the cores were shut in for 24 hours with all inlets and outlets closed.

Water Chase Floods. Water chase floods were performed to measure the blocking capacity of the gel present in the fractures. We used high-salinity brine, with the same composition as the gel solvent. A schematic of the experimental setup for gel placement and chase waterflooding may be viewed in Fig. 2.

The water-injection rate was initially low at 6 cm^3/h to accurately measure the rupture pressure (the pressure at which the gel in the fracture breaks and allows fluids to flow through it). When the differential pressure across the fracture stabilized after gel rupture, eight sequential waterflood cycles were performed in the sandstone core: The water-flow rate was first increased stepwise from 6 to 60 to 300 to 600 cm^3/h (termed “an increasing-rate cycle”) and thereafter reduced in the same manner (termed “a

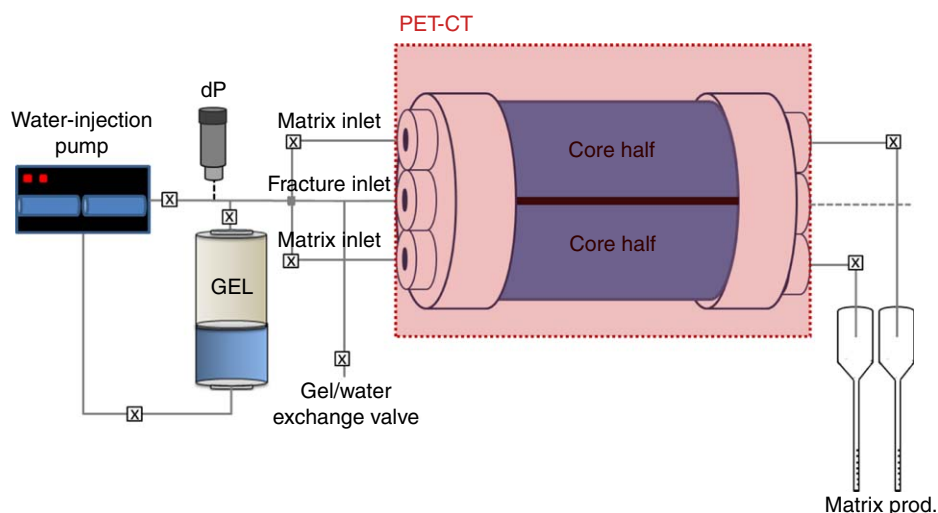


Fig. 2—Schematic of the experimental setup for gel placement and chase waterflooding. Pressure and volumetric measurements or in-situ imaging by PET were used to quantify gel behavior.

decreasing-rate cycle”). The limestone core was imaged in the PET scanner during waterflooding to visualize and quantify the flow of water through the gel-filled fracture. Two sequential waterflood cycles were performed, where the water-flow rate was first increased from 6 to 60 to 300 cm³/h, and thereafter stepwise decreased. The waterflood was thereafter left at the lowest rate (6 cm³/h) for 13 hours. The pressure across the fracture was measured as a function of time and flow rate during waterflooding for both cores, and the results from global measurements were compared with in-situ imaging. Previous work showed that gel behavior during chase floods, after mature polymer-gel placement in a fracture, is stable and predictable (Brattekkås et al. 2015a, 2015b). Although waterfloods through the sandstone core were not imaged, the measurements of pressure and rate during chase floods corroborate the measurements for the limestone core, and ensure that the conclusions reached from in-situ PET imaging are valid and descriptive of general gel behavior.

PET Imaging. A small-animal PET-CT scanner was used for in-situ imaging during chase waterflooding in the limestone core plug. Fack et al. (2015) and Haldorsen et al. (2015) used the same PET-CT for preclinical studies in rats and mice, and the experimental procedure for PET imaging was adapted for use in core plugs (Fig. 3): ¹⁸F was produced by a local cyclotron and used to synthesize ¹⁸F-fluorodeoxyglucose (¹⁸F-FDG), which is a water-soluble fluorine radioisotope with a half-life of $t_{1/2} = 109$ minutes. Spatial fluid saturations in the core plug and fracture were calculated on the basis of the registered activity of the labeled brine phase at given timesteps. PET-CT sequences were acquired on a CT 80 W Nanoscan PC imager, featuring spatial resolutions of 800 μm and 30 μm of the respective PET- and CT-detector systems (Haldorsen et al. 2015). The PET field of view (FOV) was 9.5 × 8 cm in axial and transaxial directions, allowing imaging of the entire core plug and most of the end pieces. The PET detectors consist of LYSO crystals, and acquisition was performed in 1:5 coincidence and normal count mode. A CT scan (helical projections with tube energy of 70 kVp, exposure time of 300 ms, 720 projections, max FOV, binning 1:4) was acquired for core-plug positioning; the tube voltage was, however, not high enough to correctly reproduce the spatial core-plug density, and attenuation correction from CT during PET-data reconstruction was therefore not applied. During initial waterflooding, ¹⁸F-FDG was mixed in 300 cm³ of brine at 151 MBq activity, and PET was acquired for 2 hours during stepwise alteration of the water-injection rate. After 12 hours of continuous waterflooding, ¹⁸F-FDG at 183 MBq activity was mixed in a new batch of brine (300 cm³) and injected into the fracture. PET was acquired for 1 hour during continued low-rate waterflooding.

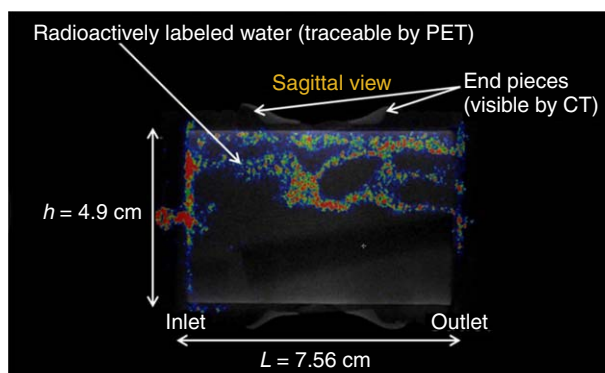


Fig. 3—View inside the longitudinal, vertically aligned fracture of the limestone core plug placed in the PET-CT scanner. The gray outline is the CT image of the core (used for positioning). Bedding planes in the rock surface may be observed as darker features, and were constant in all images. The colored signal is water-labeled with ¹⁸F-FDG, and recorded by PET.

Results and Discussion

Polymer-Gel Placement. The rate of water leakoff during gel propagation through open fractures was measured in several previous publications (Seright 2003a, 2003b; Brattekkås et al. 2015a, 2015b) and shown to be: (1) independent of core material (for fully water-saturated core plugs) and (2) largely independent of the gel-injection rate. Seright (2003b) found that, when using short fractures, screenout of gel (where concentrated gel is flushed out of the fracture caused by turbulent flow) could occur at high gel-flow rates (>2000 cm³/h). In this study, lower, constant injection rates of 200 cm³/h (for the limestone) and 6 cm³/h (for the sandstone) were used. The limestone core [porosity $\phi = 22.9\%$ and permeability $K = 13$ md (Haugen et al. 2008)] was mounted in the PET scanner during gel injection, and volumetric measurements for leakoff calculation were not performed. The leakoff rate measured during gel injection into the sandstone core ($\phi = 23\%$ and $K = 1.2$ D) was lower than expected from the leak-off models (see Fig. 4, left). The measured differential pressure across the fractures during gel injection is shown in Fig. 4, right.

Chase Waterfloods. *Calculations on the Basis of Global Measurements.* Waterflooding was performed to measure the gel blocking capacity and to analyze the development of wormholes through the gel-filled fractures. The differential pressure across the fractures was logged during waterfloods for the two core plugs

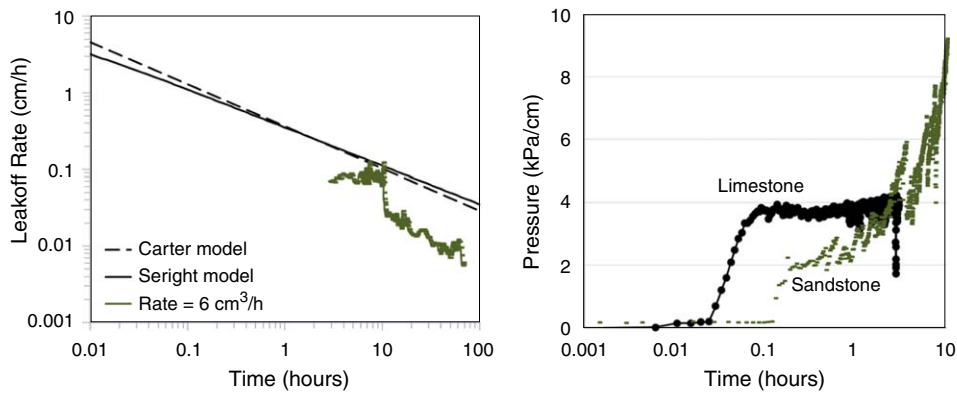


Fig. 4—Left: Measured leakoff rate for the sandstone core. Right: Differential pressure during gel injection at $200 \text{ cm}^3/\text{h}$ and $6 \text{ cm}^3/\text{h}$ into the fractured core plugs.

and formed, together with rate data, the basis for calculations and comparisons in this section.

Rupture pressures were 4.5 kPa/cm and 4.4 kPa/cm for the sandstone and limestone core, respectively, and corresponded well with previously reported rupture-pressure data after formed gel placement in fractures (Brattekkås et al. 2015a, 2015b). When the gel ruptures, water may again flow through the fracture by following the rupture path (according to the Seright leakoff model, the rupture path will be the randomly distributed wormholes through concentrated gel); measuring the pressure drop and flow rate during chase waterfloods through gel-filled fractures gives an estimate of gel behavior. In the sandstone core, eight increasing and decreasing rate cycles were performed, whereas two cycles were performed in the limestone core: one increasing-rate and one decreasing-rate cycle. The pressure gradients measured during water injection at the specific rate steps ($6 \text{ cm}^3/\text{h}$, $60 \text{ cm}^3/\text{h}$, $300 \text{ cm}^3/\text{h}$, and $600 \text{ cm}^3/\text{h}$) are shown in Fig. 5 as functions of the effective brine velocity through the fracture. The measurements were taken for each rate step when the pressure response across the gel-filled fracture had stabilized at a close-to-constant value. Fig. 5 (left) shows the initial rupture pressure and the following pressure response during the first two increasing-decreasing-rate cycles in both core plugs. The rupture pressures are denoted by a red dot (limestone) and a black triangle (sandstone) in the figure. The gel behavior during chase waterflooding was similar in the two core plugs: After gel rupture, water could pass through the fracture and the pressure gradient across the fracture decreased for the lowest water-flow rate. When the flow rate was increased

to $60 \text{ cm}^3/\text{h}$, the measured pressure gradient across the fracture continued to decrease, probably caused by further erosion of gel around the wormholes formed in the fracture. Increasing the flow rate further, to $300 \text{ cm}^3/\text{h}$ and $600 \text{ cm}^3/\text{h}$, yielded an increase in the measured pressure gradient up to the initial post-rupture level. When the flow rate was stepwise decreased back toward $6 \text{ cm}^3/\text{h}$, significantly lower pressure gradients were measured for each specific rate. This was expected behavior, attributed to erosion of gel in the wormholes during water injection.

With the water-flow rate back at the initial level ($6 \text{ cm}^3/\text{h}$), two different waterflood schedules were performed in the core plugs: In the limestone core, low-rate waterflooding was continued for 13 hours, whereas six additional decreasing-increasing-injection-rate cycles were performed in the sandstone core. Fig. 5 (right) shows the first five increasing-decreasing-rate cycles in the sandstone core, out of eight cycles in total. The pressure gradients for each specific rate continued to decrease during the third cycle (increasing rate), with respect to the first two cycles. From the third cycle, however, the pressure gradients remained on the same level within each flow rate, suggesting a stable system with minor gel erosion, although more than 120 fracture volumes (FVs) of water had passed through the fracture at this point. The elasticity of the gel enabled it to maintain a stable and high-pressure resistance after rupture and significant water throughput, because wormholes are allowed to collapse and reopen during waterflooding depending on the water-flow rate.

The development of wormholes during chase floods could be estimated from the measured differential pressure and rate data

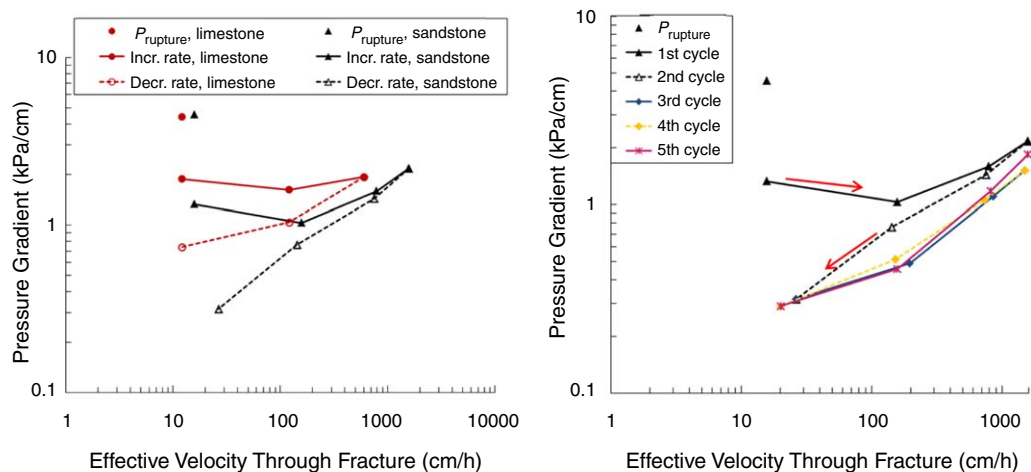


Fig. 5—Measured pressure gradients as functions of the effective velocity of brine through the fractures. Left: The limestone core (red curves) and the sandstone core (black curves) during the first two increasing- and decreasing-rate cycles. The dotted lines represent decreasing rate cycles, and the solid lines represent cycles where the injection rate increases. Right: The first five increasing-decreasing-rate cycles, out of eight in total, for the sandstone core.

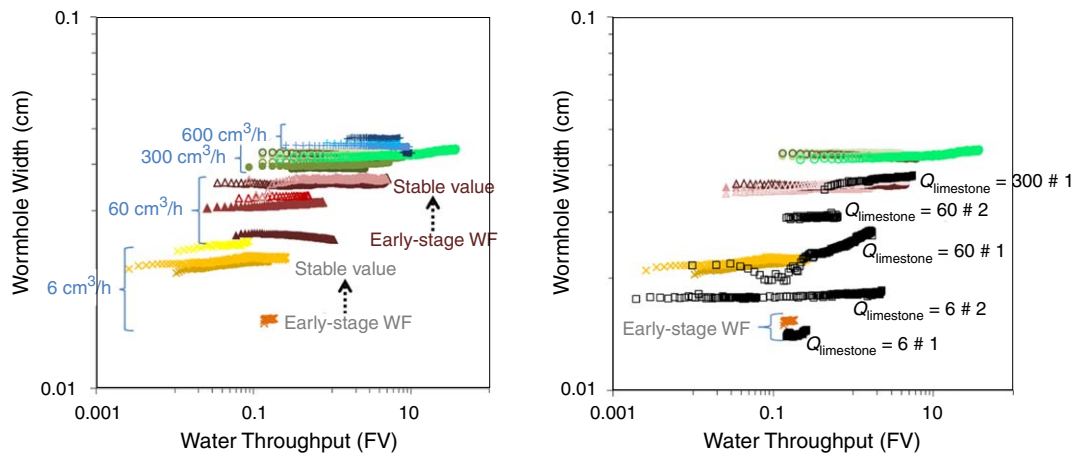


Fig. 6—Wormhole widths on the basis of calculations from global measurements. Left: Wormhole width (y -axis) as a function of water throughput at different injection rates for the sandstone core. Early-stage waterflooding yields lower wormhole widths for each injection rate. After several waterflood cycles, the wormholes stabilize at larger widths caused by minor gel erosion. The wormhole width generally increases with an increase in injection rate and decreases with a decrease in injection rate, caused by the elasticity of the gel filter cake and the wormhole ability to collapse and reopen. Right: The black squares show the calculated wormhole widths for the limestone core, compared with the stabilized wormhole widths for the sandstone core. Q denotes the specific rate for each curve.

for the two cores, by calculating the average wormhole width. The wormhole width is, in the following, defined as the average, effective channel width open to flow after gel rupture, and was calculated by Poiseuille's law. The following assumptions were made:

- For this calculation, there is only one wormhole present in the fracture. The wormhole is uniform (equal diameter throughout the fracture) and spans from the fracture inlet to the fracture outlet.
- Fluid flow will occur only through the wormhole and not through the concentrated gel in the fracture.
- The wormhole is assumed to be of cylindrical shape; thus, the calculation is valid only for as long as the wormhole width (the diameter of the cylinder) is less than the fracture aperture (0.1 cm for the cores used in this study).

Fig. 6 (left) shows the calculated wormhole width as a function of water throughput for the sandstone core plug. The wormhole width increased with increasing injection rates. A spread within each specific rate was also observed; this was expected because the calculations, by Poiseuille's law, are directly linked to the pressure drop across the fracture, which also requires some time and water throughput to stabilize (Fig. 5). Initially, the wormhole width increased with water throughput, caused by gel erosion, and thereafter stabilized at a close-to-constant value for each given rate. The wormhole width stabilized after the third waterflood cycle, and was, on average, calculated to be 0.022 cm ($6 \text{ cm}^3/\text{h}$), 0.036 cm ($60 \text{ cm}^3/\text{h}$), 0.043 cm ($300 \text{ cm}^3/\text{h}$), and 0.045 cm ($600 \text{ cm}^3/\text{h}$). Fig. 6 (right) shows the calculated wormhole width for the limestone core plug (black squares), compared with the results for the sandstone core plug when the wormholes had stabilized. Wormhole development was similar in the gel-filled fracture of the limestone core plug, and the wormhole width increased with injection rate: However, because of limited water throughput, lower wormhole widths were observed during the increasing- and decreasing-rate cycles compared with the stabilized values of the sandstone core, reached after three waterflood cycles. Two waterflood cycles were performed in the limestone core, and the stepwise adjustments in rate continued for 2 hours of water injection: At this time, the system was not fully stabilized, and further gel erosion may be expected to occur. The calculated wormhole widths were 0.018 cm ($6 \text{ cm}^3/\text{h}$), 0.029 cm ($60 \text{ cm}^3/\text{h}$), and 0.037 cm ($300 \text{ cm}^3/\text{h}$) for the limestone core, which corresponds well with early-stage waterflooding in the sandstone core. During continued low-rate waterflooding, the differential pressure across the fracture was slowly decreasing, indicating further gel erosion. After significant water throughput (13 hours and >40

FV), the wormhole width was calculated to be 0.048 cm and comparable to the wormhole width at the highest degree of gel erosion in the sandstone core. The similar development in the data for the two cores indicates that gel behavior visualized and quantified by PET in the next section (for the limestone core only) is representative for waterflooding after formed gel placement in an open fracture.

In-Situ Investigations of Wormhole Development With PET. PET imaging was used to investigate water flow through a gel-filled fracture in situ. Injection brine was labeled by ^{18}F -FDG before waterflooding; it was therefore possible to visualize and quantify the spatial saturation of water through the fracture by PET, as a function of flow rate and time. To closely investigate the water-flow pattern during the increasing- and decreasing-rate cycles, six images were constructed from the PET data—one for each rate step. The images were constructed by extracting the PET signal for each rate when the pressure drop across the core was constant and assuming a constant wormhole structure. A 2D, sagittal (view within longitudinal fracture), image was created from the 3D data set at each timestep. In this experiment, flow of radioactive fluids only occurred within the FV, and the matrix fluids did not exhibit a signal detectable by PET. The effective depth resolution in this case is therefore equal to the fracture aperture (0.1 cm). Fig. 7 shows the wormhole flow patterns at different rate stages during the waterflood; view is within the longitudinal fracture (sagittal view).

Wormholes and wormhole development with flow rate were clearly seen on the PET images. Fig. 7 shows the wormhole formed during initial waterflooding at $6 \text{ cm}^3/\text{h}$ (left image, top row). The wormhole mostly consists of a single flow conduit at this point, although large-scale variations in the size of the rupture path were observed within the FV. 11% of the FV emitted a radioactive signal (i.e., conducted flow of radioactive water), and thus contained wormhole(s). The rest of the fracture was filled with concentrated gel that did not exhibit a signal detectable by PET. When the rate was increased to $60 \text{ cm}^3/\text{h}$ (Fig. 7, center image, top row), the wormhole branched out and filled larger portions of the fracture. New rupture paths were formed through the concentrated gel filter cake compared with the first rate step, and fluid flow was observed through several wormholes spanning between the inlet and outlet. The 22% of the FV conducted water flow at $60 \text{ cm}^3/\text{h}$, efficiently doubling the wormhole volume since gel rupture. The part of the FV conducting flow of radioactive water (i.e., the wormhole volume) increased further (27%) when the injection rate was increased to $300 \text{ cm}^3/\text{h}$ (Fig. 7, right image, top row), although at a much lower scale. New wormhole flow paths were

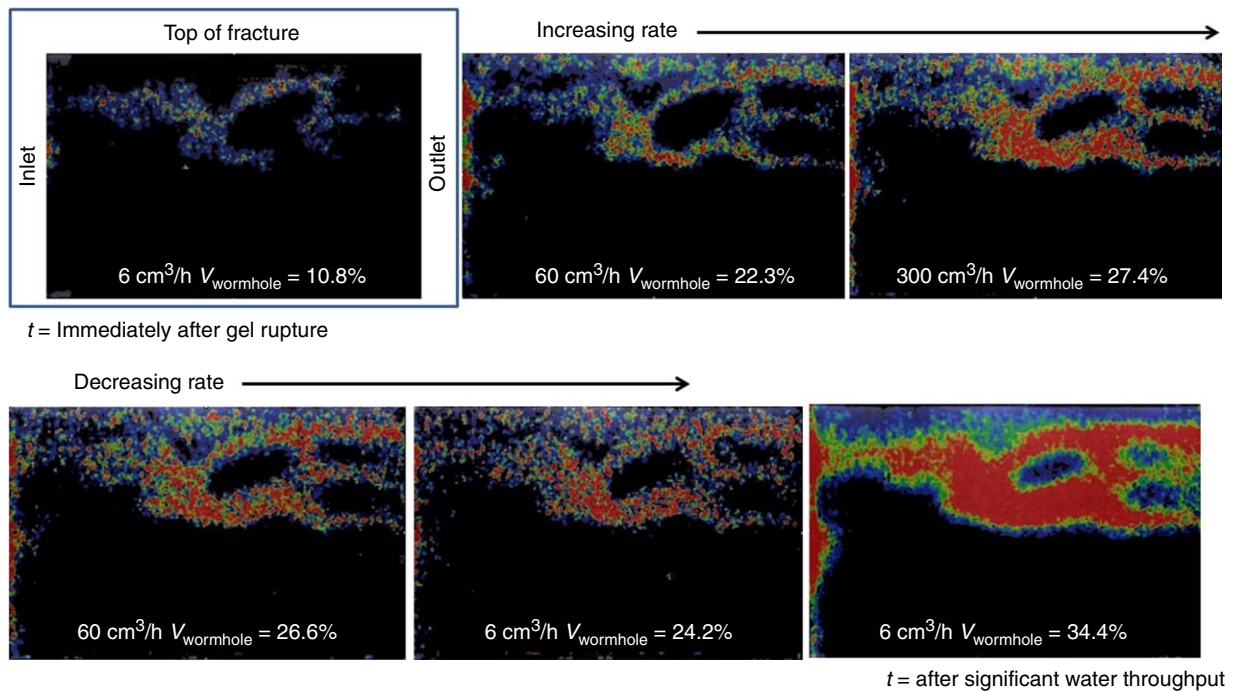


Fig. 7—PET images showing the formation of wormholes during chase waterflooding. The colored signal is water traced with radioactive pharmaceutical ^{18}F -FDG. The fracture was vertically aligned, and the top of the images corresponds to the top of the fracture. The first image (top, left) shows the wormhole flow path immediately after gel rupture at $6\text{ cm}^3/\text{h}$. The next two rate increases were $60\text{ cm}^3/\text{h}$ (top, middle) and $300\text{ cm}^3/\text{h}$ (top, right), during which the wormhole flow pattern was extended. Stepwise decreasing the rate to $60\text{ cm}^3/\text{h}$ (bottom, left) and $6\text{ cm}^3/\text{h}$ (bottom, middle) did not change the flow pattern back to one single conduit. The wormhole flow pattern after significant water throughput (bottom, right) was extended because of gel erosion.

not created during this rate step, indicating that the increased wormhole volume was caused by erosion of gel around existing wormholes. Fig. 7 (lower row) shows the decreasing-rate cycle. A reduction in the rate to $60\text{ cm}^3/\text{h}$ did not cause a corresponding reduction in the measured wormhole volume, and the wormhole remained in the same shape and location as in the previous rate step. Reducing the flow rate to $6\text{ cm}^3/\text{h}$ reduced the wormhole volume to 24% of the FV, without changing the wormhole morphology. Fig. 7 (right image, lower row) shows the wormhole flow path after significant water throughput at $6\text{ cm}^3/\text{h}$, where wormholes covered 34% of the FV.

In-situ imaging supported the existence of a nonuniform gel filter cake in the fracture, and we observed that (for the first two waterflood cycles) (1) the wormholes are in the same location from the initial breach to late waterflooding; (2) the wormholes are, for the most part, in the same shape for the duration of waterflooding, although new rupture paths were added to the original rupture path when the flow rate was increased above the original level; (3) the wormholes are eroded wider when higher and higher rates are used; (4) but the wormholes do not collapse when the rate is lowered; and (5) extended waterflooding substantially erodes gel along the fracture-width direction but does not form new wormhole pathways.

Wormhole Development: In-Situ Measurements Compared to Global Calculations. We converted the total measured wormhole volume in the fracture by PET, given in the previous section, to average wormhole widths with simple calculations of geometry: For simple comparison, we again assumed that there was only one wormhole in the fracture, and that it spanned the length of the fracture. The assumed wormhole had a rectangular shape, where one side was fixed at the fracture aperture and the other side was the wormhole width (W_w) (not fixed). The wormhole was thus envisioned to expand and retract vertically within the FV (i.e., in the largest dimension of the fracture). In-situ imaging by PET (e.g., Fig. 7) showed large variations in the wormhole width, from very narrow (almost invisible on images) in some sections of the fracture to spanning almost half the fracture height in other sections. Extracting an average value for the wormhole width from

the PET images therefore holds a large degree of uncertainty. However, it was necessary to find these values to be able to compare in-situ imaging to calculations from global measurements. We found that measured average wormhole widths by PET were more than thirty times higher than the calculated values for each specific injection rate; the data are shown and compared in Fig. 8. The high average wormhole widths measured by PET therefore do not account for the high pressure gradients achieved during post-rupture waterflooding. This indicates that the average wormhole width is not a good measure for the actual conductivity of the fracture, and is not the controlling factor for flow. The difference in wormhole morphology is an important distinction between calculations and measurements that may explain this deviation: The basis for calculations was a single, uniform wormhole spanning from the fracture inlet to the fracture outlet, and assumed to be the only conductor for flow. In-situ imaging by PET revealed the existence of several wormholes, seemingly randomly distributed within the FV, and with significant variations in width. Image-analysis software ImageJ (<https://imagej.nih.gov/ij/>) identified the smallest wormhole width (where the signal was barely visible on the images) to be 0.001 cm, which was less than all calculated values from global measurements (Fig. 8, right). Narrow constrictions in the wormhole flow paths will act as natural chokes on fluid production and control the pressure response across the fracture during subsequent floods. This mechanism is only possible when the filter cake forming in the fracture during gel placement is heterogeneous; thus, the paths of gel rupture during subsequent floods (presumably in wormholes) are naturally nonuniform and dependent on local gel concentration. In many previous publications, pressure-drop and rate data are the only available tools to investigate wormhole development during chase floods, and wormhole width is calculated on the basis of the same assumptions as in this work. In-situ imaging by PET shows that the single, uniform wormhole assumed in the calculations is not descriptive of fluid flow through the gel-filled fracture. Knowledge of the wormhole morphology and development is important when planning integrated EOR (iEOR) operations, because the success of a chase flood will largely depend on the ability of the

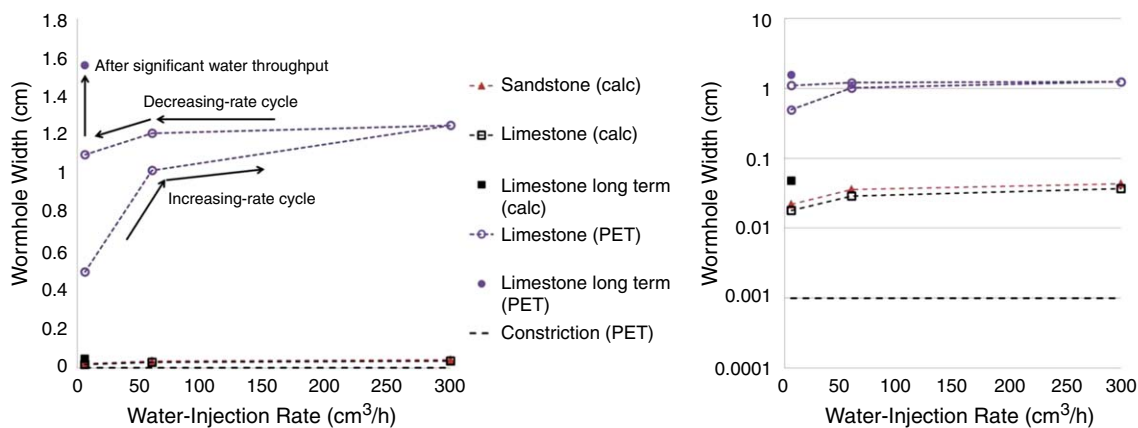


Fig. 8—Left: Calculated wormhole width from pressure measurements compared with measured wormhole width from in-situ imaging by PET. Right: Calculated wormhole width from pressure measurements compared with measured wormhole width from in-situ imaging by PET. Logarithmic scale on the y-axis for improved comparison: The dotted line denoted “constriction PET” is the smallest wormhole width measured by PET at all injection rates.

chase fluid to dilate or constrict the narrow sections of a wormhole.

Average gel concentration varies with lengthwise position in a fracture, with higher concentrations close to the fracture inlet and a decreasing concentration toward the fracture outlet. For the limestone core, a clear relationship between fracture position and wormhole width was not found, possibly because of the use of a short fracture. For all rate steps, the narrow flow paths were found close to the fracture inlet and outlet, and the largest wormhole widths were measured in the second and third quarters of the fracture length.

Advantages of In-Situ Imaging. Several previous publications have supported the existence of a nonuniform gel filter cake in the fracture after formed gel placement: Seright (2003b) injected dyed gel to follow gel of the same composition (not dyed) into a fracture, and observed that gel of injected composition flowed through concentrated gel in wormholes during gel placement, shown in Fig. 9 (left). Brattekkås et al. (2015a, 2015b) observed clearly visible wormhole patterns resulting from chase waterfloods when gel-filled fractures were opened and fracture surfaces inspected after chase waterflooding (Fig. 9, center). The development of wormholes during dynamic chase waterfloods was investigated by PET in this study (Fig. 9, right) with clear advantages: In-situ imaging by PET only relied on the presence and decay of radioactive water in the core, and could be performed during dynamic floods for several different flow rates and time-steps. PET is able to catch and quantify quick changes in polymer-gel networks during chase waterfloods without damaging the core or gel; thus, the core can be used further in experiments. Visual inspection of fracture surfaces, as in Fig. 9 (middle), requires the

core to be broken apart, and the core cannot be used further (e.g., to investigate and compare EOR chase floods to already-performed water chase floods). In addition, the observations made are highly qualitative, and dynamic changes resulting from differences in pressure and rate are not captured. In-situ imaging by PET will be used in future work to augment previous experiments on, for example, the effect of gel state during placement and the mechanism behind low-salinity waterfloods for improved high-salinity gel blocking (Brattekkås et al. 2015a, 2015b).

Conclusions

- In-situ imaging by PET is a good and efficient method for investigating water chase floods through gel-filled fractures.
- We used PET to investigate the development of wormholes during dynamic waterfloods. PET imaging supported the existence of a nonuniform gel filter cake in the fracture.
- The wormhole width, measured by PET, varied significantly within the FV, and did not correspond to calculated values from pressure and rate data.
- The average wormhole width measured by PET is not a good indication of fracture flow capacity. Fracture flow and pressure response across the fracture are controlled by narrow constrictions in the wormhole flow path.
- Wormholes covered 11% of the FV immediately after gel rupture, visualized by PET.
- New rupture paths (wormholes) were added to the original gel-rupture path when the water-flow rate was increased above the initial level.

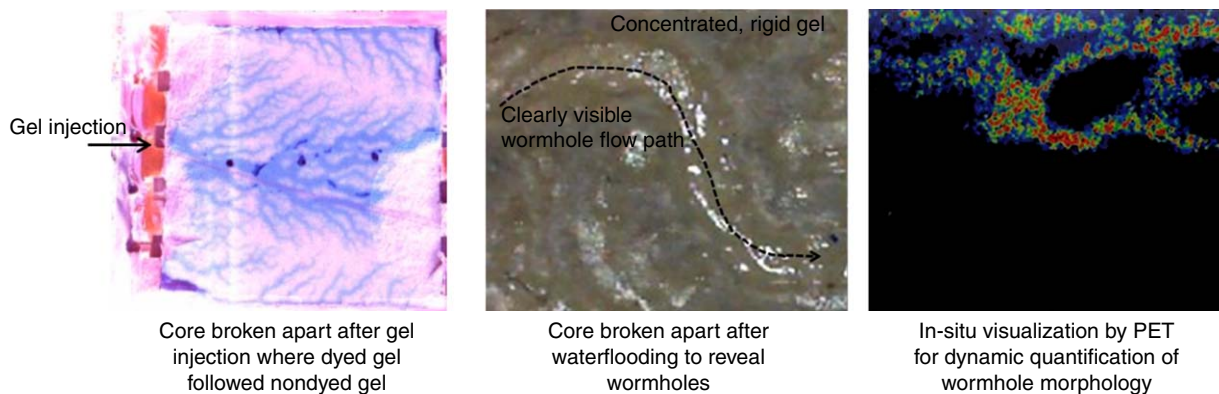


Fig. 9—Left: Dyed-gel injection following gel of the same composition (not dyed) from Seright (2003b). Center: Clearly visible wormhole after waterflooding from Brattekkås et al. (2015a, 2015b). Right: PET imaging of a complete wormhole flow pattern in a gel-filled fracture still intact.

- After the wormhole(s) had expanded, they remained in the same shape and location for the entire waterflood, and changes in the wormhole volume with rate were attributed to gel erosion (during increasing-rate cycles) and gel elasticity (wormholes collapsing during decreasing-rate cycles).
- Wormhole collapse was not significant during the two increasing-decreasing-rate cycles performed in the limestone core.
- Extended waterflooding was observed to substantially erode the gel along the fracture-width direction, however, without forming new wormhole pathways.
- The high initial pressure response of the gel was not restored after rupture and significant water throughput. A high pressure level was, however, maintained for the sandstone core during several increasing-decreasing-rate cycles when gel erosion had stabilized after three consecutive rate cycles.

Acknowledgments

The PET-CT scanner was used in collaboration with the Molecular Imaging Centre (MIC), Department of Biomedicine, University of Bergen, Norway. The authors wish to acknowledge senior engineer Cecilie Brekke Rygh for training.

The authors acknowledge the Research Council of Norway and the industry partners—ConocoPhillips Skandinavia A–S, BP Norge A–S, Det Norske Oljeselskap A–S, Eni Norge A–S, Maersk Oil Norway A–S, Dong Energy A/S Denmark, Statoil Petroleum A–S, GDF SUEZ E&P Norge A–S, Lundin Norway A–S, Halliburton A–S, Schlumberger Norge A–S, and Wintershall Norge A–S—of The National IOR Centre of Norway for support.

References

Benham, A. L. and Olson, R. W. 1963. A Model Study of Viscous Fingering. *SPE J.* **3** (2): 138–144. SPE-513-PA. <http://dx.doi.org/10.2118/513-PA>.

Brattekkås, B., Pedersen, S. G., Nistov, H. T. et al. 2015a. Washout of Cr(III)-Acetate-HPAM Gels From Fractures: Effect of Gel State During Placement. *SPE Prod & Oper* **30** (2): 99–109. SPE-169064-PA. <http://dx.doi.org/10.2118/169064-PA>.

Brattekkås, B., Graue, A., and Seright, R. S. 2015b. Low-Salinity Chase Waterfloods Improve Performance of Cr(III)-Acetate Hydrolyzed Polyacrylamide Gel in Fractured Cores. Presented at the SPE International Symposium on Oilfield Chemistry, The Woodlands, Texas, 13–15 April. SPE-173749-MS. <http://dx.doi.org/10.2118/173749-MS>. [See also *SPE Res Eval & Eng* **19** (2): 331–339, SPE-173749-PA.]

Ekdale, A. A. and Bromley, R. G. 1983. Trace Fossils and Ichnofabric in the Kjølbj Gaard Marl, Uppermost Cretaceous, Denmark. *Bull Geol. Soc. Denmark* **31**: 107–119.

Ersland, G., Ferno, M. A., Graue, A. et al. 2010. Complementary Imaging of Oil Recovery Mechanisms in Fractured Reservoirs. *Chemical Engineering Journal* **158**: 32–38. <http://dx.doi.org/10.1016/j.cej.2008.11.049>.

Fack, F., Keunen, O., Espedal, H. et al. 2015. Bevacizumab Treatment Induces Metabolic Adaption Toward Anaerobic Metabolism in Glioblastomas. *Acta Neuropathologica* **129**: 115–131. <http://dx.doi.org/10.1007/s00401-014-1352-5>.

Fernø, M. A., Gauteplass, J., Hauge, L. P. et al. 2015a. Combined Positron Emission Tomography and Computed Tomography To Visualize and Quantify Fluid Flow in Sedimentary Rocks. *Water Resour. Res* **51** (9): 7811–7819. <http://dx.doi.org/10.1002/2015WR017130>.

Fernø, M. A., Haugen, A., Brattekkås, B. et al. 2015b. Quick and Affordable SCAL: Spontaneous Core Analysis. Presented at the International Symposium of the Society of Core Analysts, St. John's, Newfoundland and Labrador, Canada, 16–21 August. SCA2015-003.

Ganguly, S., Willhite, G. P., Green, D. W. et al. 2002. The Effect of Fluid Leakoff on Gel Placement and Gel Stability in Fractures. *SPE J.* **7** (3): 309–315. SPE-79402-PA. <http://dx.doi.org/10.2118/79402-PA>.

Haldorsen, I. S., Popa, M., Fonnes, T. et al. 2015. Multimodal Imaging of Orthopic Mouse Model of Endometrial Carcinoma. *PLoS ONE* **10** (8): e0135220. <http://dx.doi.org/10.1371/journal.pone.0135220>. eCollection.

Haugen, Å., Fernø, M. A., and Graue, A. 2008. Numerical Simulation and Sensitivity Analysis of In-Situ Fluid Flow in MRI Laboratory Water-

floods of Fractured Carbonate Rocks at Different Wettabilities. Presented at the SPE Annual Technical Conference and Exhibition, Denver, 21–24 September. SPE-116145-MS. <http://dx.doi.org/10.2118/116145-MS>.

Howard, G. C. and Fast, C. R. 1957. Optimum Fluid Characteristics for Fracture Extension. In *Drilling and Production Practices*, API-47-261. New York, New York: API.

Howard, G. C. and Fast, C. R. 1970. *Hydraulic Fracturing*. Vol. 2. Richardson, Texas: Monograph Series, Society of Petroleum Engineers.

Klein, E. and Reuschle, T. 2003. A Model for the Mechanical Behaviour of Bentheim Sandstone in the Brittle Regime. *Pure Applied Geophysics* **160**: 833–849. <http://dx.doi.org/10.1007/PL00012568>.

Liu, Y. 2006. *Settling and Hydrodynamic Retardation of Proppants in Hydraulic Fractures*. PhD dissertation, The University of Texas at Austin (August 2006).

Maucec, M., van Heerden, M., Dusterhoft, R. et al. 2013. Imaging of Fluid Mobility in Fractured Cores Using Time-lapse Positron Emission Tomography. Presented at the SPE Annual Technical Conference and Exhibition, New Orleans, 30 September–2 October. SPE-166402-MS. <http://dx.doi.org/10.2118/166402-MS>.

Penny, G. S. and Conway, M. W. 1989. Fluid Leakoff. In *Recent Advances in Hydraulic Fracturing*, eds. J. L. Gidley, S. A. Holditch, D. E. Nierode, and R. W. Veatch Jr., Vol. 12, Chapter 8, 147–176. Richardson, Texas: Monograph Series, Society of Petroleum Engineers.

Portwood, J. T. 1999. Lessons Learned From Over 300 Producing Well Water Shut-Off Gel Treatments. Presented at the SPE Mid-Continent Operations Symposium, Oklahoma City, Oklahoma, 28–31 March. SPE-52127-MS. <http://dx.doi.org/10.2118/52127-MS>.

Schutjens, P. M. T. M., Hausenblas, M., Dijkshoorn, M. et al. 1995. The Influence of Intergranular Microcracks on the Petrophysical Properties of Sandstone—Experiments To Quantify Effects of Core Damage. Presented at the International Symposium of the Society of Core Analysts, San Francisco, California. SCA-9524.

Seright, R. S. 1999. Polymer Gel Dehydration During Extrusion Through Fractures. *SPE Prod & Fac* **14** (2): 110–116. SPE-56126-PA. <http://dx.doi.org/10.2118/56126-PA>.

Seright, R. S. 2001. Gel Propagation Through Fractures. *SPE Prod & Fac* **16** (4): 225–231. SPE-74602-PA. <http://dx.doi.org/10.2118/74602-PA>.

Seright, R. S., Lane, R. H., and Sydansk, R. D. 2003. A Strategy for Attacking Excess Water Production. *SPE Prod & Fac* **18** (3): 158–169. SPE-84966-PA. <http://dx.doi.org/10.2118/84966-PA>.

Seright, R. S. 2003a. Washout of Cr(III)-Acetate-HPAM Gels From Fractures. Presented at the International Symposium on Oilfield Chemistry, Houston, 5–7 February. SPE-80200-MS. <http://dx.doi.org/10.2118/80200-MS>.

Seright, R. S. 2003b. An Alternative View of Filter-Cake Formation in Fractures Inspired by Cr(III)-Acetate-HPAM Gel Extrusion. *SPE Prod & Fac* **18** (1): 65–72. SPE-81829-PA. <http://dx.doi.org/10.2118/81829-PA>.

Siddhartha, S. and Morrow, N. R. 2007. Efficiency of the Conversion of Work of Drainage to Surface Energy for Sandstone and Carbonate. *SPE Res Eval & Eng* **10** (4): 338–347. SPE-102490-PA. <http://dx.doi.org/10.2118/102490-PA>.

Willhite, G. P. and Pancake, R. E. 2008. Controlling Water Production Using Gelled Polymer Systems. *SPE Res Eval & Eng* **11** (3): 454–465. SPE-89464-PA. <http://dx.doi.org/10.2118/89464-PA>.

Bergit Brattekkås is currently a post-doctoral-degree researcher at the National IOR Centre of Norway at the University of Stavanger. She has previously worked as a researcher at the National IOR Centre of Norway, as a research fellow at the University of Bergen, and as a visiting researcher at the Petroleum Recovery Research Center of New Mexico Tech. Brattekkås' research interests are EOR and flow mechanisms in mature oil reservoirs (e.g., increasing sweep efficiency by injection of polymer gels or foam). She holds MSc and PhD degrees in reservoir physics from the University of Bergen.

Marianne Steinsbø is a senior engineer at the Department of Physics and Technology, University of Bergen. She has previously worked as a researcher with Epsis A–S. Steinsbø's

research interest is EOR in heterogeneous and fractured reservoirs. She holds MSc and PhD degrees in reservoir physics from the University of Bergen.

Arne Graue is a professor in the Department of Physics and Technology, University of Bergen, where he is Head of the Petroleum and Process Technology Research Group. His scientific interest is within reservoir physics, emphasizing heterogeneous and fractured reservoirs, multiphase flow in porous media, in-situ fluid-saturation imaging, laboratory investigation of integrated EOR techniques, CO₂ sequestration, and gas hydrates. Graue has authored more than 200 scientific publications and has supervised more than 120 PhD and MS degree students. He holds an MS degree in experimental nuclear physics and a PhD degree in reservoir physics, all from the University of Bergen.

Martin A. Fernø is an associate professor in the Petroleum and Process Technology research group at the Department of Physics and Technology, University of Bergen. His research focuses on flow, oil recovery, and carbon dioxide (CO₂) storage in heterogeneous, fractured reservoirs with emphasis on

in-situ imaging. Fernø's scientific interests include spontaneous imbibition, foam flow, and combined CO₂ storage and EOR. He has authored more than 80 scientific publications and supervised more than 55 PhD and MS degree students in petroleum technology at the Department of Physics and Technology. Fernø is the recipient of the 2015 Meltzer prize for outstanding young scientist at the University of Bergen and is a member of SPE.

Heidi Espedal is the manager of the preclinical PET-CT facilities at the Molecular Imaging Center at University of Bergen. Research interests include small-animal imaging methods and tracer development in PET/CT. Espedal holds a PhD degree in molecular neuro-oncology from the University of Bergen.

Randy Seright is a senior engineer at the Petroleum Recovery Research Center of New Mexico Tech in Socorro, New Mexico, where he has worked the past 28 years. He holds a PhD degree in chemical engineering from the University of Wisconsin (Madison). Seright received the SPE/DOE IOR Pioneer Award in 2008 for his work on using polymers and gels to improve oil recovery.